

Reconstructing Satellites in 3D from Amateur Telescope Images

Zhiming Chang^{1,2}, Boyang Liu³, Yifei Xia⁴, Weimin Bai¹, Youming Guo⁵, Boxin Shi⁴, He Sun^{1*}

¹College of Future Technology and National Biomedical Imaging Center, Peking University

²College of Engineering, Peking University, Beijing, China

³Earthrise Edu&Tech, China

⁴National Key Laboratory for Multimedia Information Processing and National Engineering Research Center of Visual Technology, School of Computer Science, Peking University, Beijing, China

⁵Institute of Optics and Electronics, Chinese Academy of Sciences, Chengdu, China

{changzhiming, weiminbai}@stu.pku.edu.cn, pkulby@foxmail.com, {yfxia, shiboxin}@pku.edu.cn, guoyouming@ioe.ac.cn, hesun@pku.edu.cn

Abstract

This paper proposes a framework for the 3D reconstruction of satellites in low-Earth orbit, utilizing videos captured by small amateur telescopes. The video data obtained from these telescopes differ significantly from data for standard 3D reconstruction tasks, characterized by intense motion blur, atmospheric turbulence, pervasive background light pollution, extended focal length and constrained observational perspectives. To address these challenges, our approach begins with a comprehensive pre-processing workflow that encompasses deep learning-based image restoration, feature point extraction and camera pose initialization. We apply a customized Structure from Motion (SfM) approach, followed by an improved 3D Gaussian splatting algorithm, to achieve high-fidelity 3D model reconstruction. Our technique supports simultaneous 3D Gaussian training and pose estimation, enabling the robust generation of intricate 3D point clouds from sparse, noisy data. The procedure is further bolstered by a post-editing phase designed to eliminate noise points inconsistent with our prior knowledge of a satellite’s geometric constraints. We validate our approach on synthetic datasets and actual observations of China’s Space Station and International Space Station, showcasing its significant advantages over existing methods in reconstructing 3D space objects from ground-based observations.

1. Introduction

The monitoring of man-made objects in space is an essential endeavor in space domain awareness (SDA), par-

*Corresponding author.

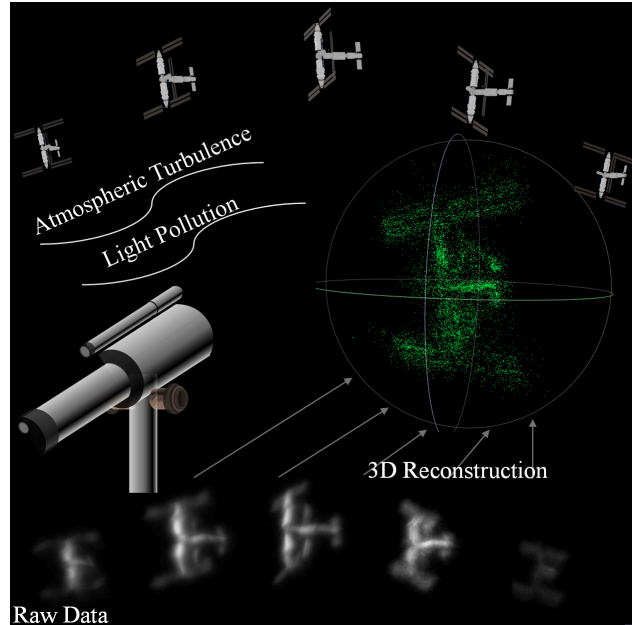


Figure 1. Problem definition. Our objective is to reconstruct a 3D model of a satellite in low-Earth orbit using limited, blurry, and noisy images captured by an amateur ground-based telescope, which are significantly affected by atmospheric turbulence and light pollution.

ticularly critical for ensuring the safe operation and on-orbit servicing of civilian satellites in the era of burgeoning large-scale satellite constellations, such as SpaceX’s Starlink [45]. Within the broad spectrum of satellite monitoring activities, including detection, categorization, and tracking, 3D reconstruction stands out as a promising advancement in the field, as it uniquely provides unparalleled insights into the real-time operational status of satellites.

To date, 3D reconstruction has predominantly been investigated in the context of space-based space surveillance missions [44], aiming to derive three-dimensional information from videos captured by neighboring satellites. Nonetheless, the potential of 3D reconstruction from ground-based observations remains markedly under-explored, despite its advantages in terms of cost-effectiveness and versatility. Unlike their space-based counterparts, ground-based observations present a series of unique challenges: 1) atmospheric turbulence significantly distorts images captured by ground telescopes; 2) the extended focal length of the ground telescope complicates the accurate estimation of a satellite’s pose; and 3) the rapid motion of satellites necessitates short exposure times, resulting in low signal-to-noise (SNR) ratios and constrained observational perspectives.

In this paper, we propose an innovative imaging approach for the 3D reconstruction of satellites using ground-based telescope images. Building on recent advances in imaging through turbulence and computer graphics volumetric rendering, we designed a cutting-edge 3D astrophotography pipeline composed of three key components: sophisticated pre-processing, a custom Structure from Motion (SfM) approach, and an improved Gaussian splatting technique [18]. This novel approach facilitates simultaneous volume reconstruction and pose estimation, while also incorporating sophisticated pre- and post-processing pipelines specifically tailored for limited, distorted, and noisy ground telescope observations. We validate our method using both simulated and experimental datasets. Notably, we achieve the successful reconstruction of 3D models of the International Space Station (ISS) and China’s Space Station (CSS, or Tiangong Station), satellites in low Earth orbit, using solely images from an amateur 35cm-aperture telescope.

2. Related Work

2.1. Spaceborne Satellite Monitoring

In space surveillance and servicing missions, accurate 3D reconstruction and pose estimation are essential for satellite maintenance, debris removal, and autonomous navigation. These tasks often rely on monocular camera observations from companion satellites due to constraints on size and power of the onboard instrument. However, traditional computer vision algorithms [25, 43] sometimes struggle to adapt to space images, because of the high noise levels, simple textures, and symmetric features of space objects.

Recent advancements have leveraged deep learning to improve spaceborne monocular pose estimation, supported by synthetic datasets like SPEED[41], SPEED+[34], and SHIRT[32]. CNN-based approaches [33, 35, 41, 51] enhanced with predefined object models (e.g., point clouds

[35] or wireframes [10, 42]) yield robust pose estimates. Recent work aims to integrate pose estimation and 3D reconstruction for monitoring unknown objects (e.g., space debris), enabling simultaneous shape and pose characterization from limited 2D images [8, 31, 50]. However, these methods typically rely on extensive synthetic training data.

2.2. Imaging through Turbulence

Ground-based observations of space objects encounter significant image quality degradation due to atmospheric turbulence, especially in amateur telescope footage. Adaptive Optics (AO) [37] is a widely used approach that actively corrects wavefront distortions in real-time using deformable mirrors, however, it is typically restricted to large observatories due to cost and complexity.

Algorithmic methods like lucky imaging [21] select frames with minimal turbulence artifacts from high-frame-rate captures, also enabling turbulence-related blur elimination [1, 2, 26]. Recent advances in turbulence simulation [7, 27, 40] have spurred deep learning methods [28, 36, 49, 52], where neural networks trained on degraded and ground-truth image pairs can predict and correct turbulence effects, outperforming classical techniques in reconstruction quality and robustness.

2.3. 3D Reconstruction and View Synthesis

3D reconstruction has traditionally relied on multi-view geometry techniques like Structure from Motion (SfM) [39]. This process begins by detecting and matching features across images (e.g., SIFT [24] or SURF), followed by camera pose estimation based on these matches [12]. A sparse 3D point cloud is then generated through triangulation, and bundle adjustment [46] are leveraged to optimize both camera and 3D point parameters. While effective, SfM struggles with noise, sparse viewpoints, and complex scene dynamics, as seen in amateur satellite imaging.

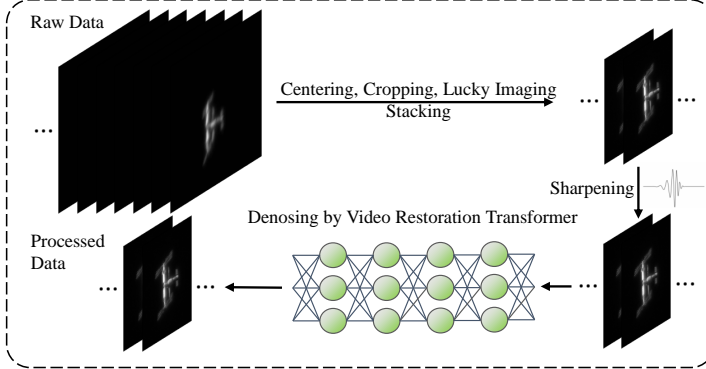
Neural Radiance Fields (NeRF) [29, 30] revolutionized 3D reconstruction and view synthesis by modeling scenes’ volumetric density and color using deep networks, enabling realistic renderings that capture intricate lighting and transparency from sparse viewpoints [4, 5, 13]. Variants like NeRF—[47], SC-NeRF[16] and BARF[23] integrate motion information inspired by SfM, allowing simultaneous 3D reconstruction and view synthesis from unposed images. However, NeRF’s dense neural network architecture limits its suitability for real-time rendering and scene editing.

3D Gaussian splatting [18] offers an efficient alternative by representing scenes with differentiable Gaussian points instead of dense neural networks. This approach accelerates rendering and allows direct scene editing by manipulating Gaussian splats [6, 11, 15]. Its flexibility and efficiency support applications like ground-based 3D satellite imaging, which requires robust reconstructions from com-

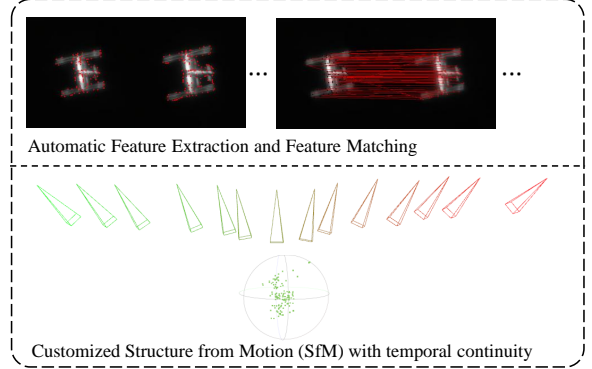
(a) Raw satellite images from ground telescopes



(b) Pre-processing: centering, lucky imaging, sharpening, and denoising



(c) Satellite's Pose and Shape Initialization



(d) Joint training of camera poses and Gaussian points to minimize the loss between rasterized images and pre-processed observations

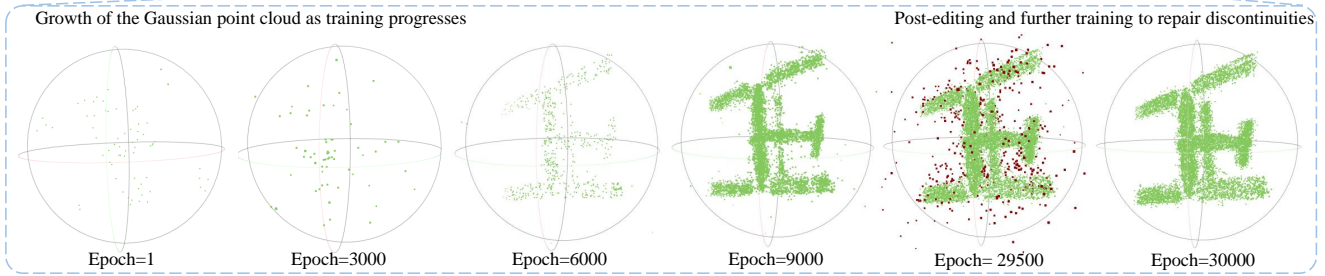
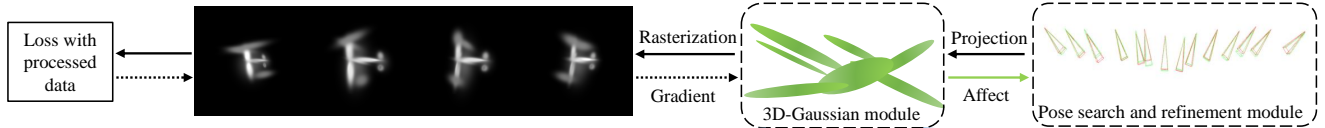


Figure 2. Overview of the 3D satellite reconstruction pipeline. This pipeline begins with the raw satellite images (a) obtained from ground-based telescopes, plagued by severe jitter, blurriness, and complex noise. Our methodology unfolds in three pivotal steps: 1) Image pre-processing (b), which incorporates techniques such as centering, lucky imaging, wavelet decomposition sharpening, and deep learning denoising; 2) Satellite’s pose and shape initialization (c), covering the robust feature extraction and matching, the pose initialization with orthographic projection, and the customized SfM with temporal continuity; 3) Joint pose refinement and 3D reconstruction (d), combining simultaneous pose refinement with 3D Gaussian training and final post-processing.

plex data.

3. Method

This paper aims to accomplish the 3D reconstruction of space objects from monocular images captured by ground-based telescopes. Unlike typical 3D reconstruction tasks, ground-based observations face challenges like atmospheric turbulence, light pollution, and limited viewpoints, as shown in Fig. 1 and Fig. 2(a). Turbulence distorts light paths, while light pollution reduces visibility, making reconstruction difficult due to constrained, distorted, blurry, and noisy images.

To overcome these challenges, we propose a 3D reconstruction approach based on the Gaussian splatting algorithm. Our approach comprises three main steps: (1) pre-processing raw telescope images (Fig. 2(b)), (2) initializing the satellite’s pose and shape with a modified SfM approach (Fig. 2(c)), and (3) joint pose refinement and 3D reconstruction using Gaussian splatting (Fig. 2(d)). Further mathematical details are provided in the supplementary materials.

3.1. Raw Telescope Images Pre-processing

Pre-processing is essential to reduce distortions and enhance image quality. Our pipeline combines analytical and

deep learning pre-processing methods in three main components:

a) Lucky imaging We apply lucky imaging[14, 19] to sequences of short-exposure images to reduce significant atmospheric distortion. This technique selects high-quality frames based on sharpness and contrast, capturing moments with minimal turbulence. These selected frames are then registered and stacked to produce high signal-to-noise ratio images.

b) Image sharpening with wavelet decomposition Stacking reduces noise but can blur high-frequency details and increase background intensity. To counteract these effects, we apply Gaussian wavelet decomposition[3] to sharpen the images by amplifying high frequencies and attenuating low frequencies to reduce background light.

c) Image enhancement with Video Restoration Transformer (VRT) Analytical sharpening often introduces unwanted noise or artifacts. To address this, we use the Video Restoration Transformer (VRT) [22], a pre-trained foundational model for video processing, to further denoise the sharpened images.

3.2. Satellite’s Pose and Shape Initialization

The next step initializes the satellite’s pose and shape using a customized SfM approach. In astrophotography, space objects move rapidly in orbit while the telescope remains fixed on Earth. For ease of applying advanced computer vision techniques, we reframe this setup in an equivalent way, treating the satellite as stationary and the telescope as if it “moves” around it. Low image quality and ultra-long focal length require specialized techniques beyond conventional SfM, which we address as follows:

a) Robust feature extraction and matching We identify and match feature points using pre-trained deep learning models, SuperPoint[9] for extraction and SuperGlue[38] for matching (Fig.2(c)). These networks demonstrate greater efficiency and robustness than conventional extractors (e.g., SIFT) when handling telescope images affected by distortion, blur, and limited textures. RANSAC regression is then applied to further filter mismatches and enhance temporal consistency.

b) Pose initialization with orthographic projection We initialize the satellite’s pose using an orthographic projection model optimized for long focal lengths [17], where minimal perspective effects make orthographic projection a better fit than traditional models. Using the Tomasi-Kanade factorization, this approach improves robustness to noise and calibration errors in narrow-angle views, where perspective models struggle with rotation and translation accuracy. This process provides initial satellite poses from the first three images and generates a preliminary feature point cloud of the satellite’s shape.

c) Customized SfM with temporal continuity We calcu-

late all camera poses and build a complete satellite point cloud using an SfM approach that integrates temporal constraints. Frames are sequentially added, with each frame’s pose estimated by matching feature points to its adjacent frames (Fig.2(c)). A global bundle adjustment then refines the poses of all processed frames. Approximately every five frames, we perform triangulation and add features from subsequent frames (e.g., the 5th and 6th, 10th and 11th) to the point cloud to minimize matching errors. This process repeats until all images are processed.

3.3. Joint pose refinement and 3D reconstruction

With initial satellite poses and shape established, we finally apply Gaussian splatting to jointly refine poses and reconstruct a high-accuracy 3D model.

a) Gaussian splatting with controlled growth This approach alternates between training Gaussian splatting parameters assuming known poses and refining camera orientations and translations using Branch and Bound (BnB) search [20] based on photometric consistency. To prevent overfitting, we manage the growth of Gaussian points: first initializing 3D Gaussian positions from the SfM-derived point cloud and training for 3,000 epochs without pose refinement, then iterating between 500 epochs of training and camera pose refinement for 10 cycles (5,000 epochs), allowing camera pose updates only at the end of each cycle. After this, point growth is halted, and we refine only existing Gaussian parameters for another 21,500 epochs.

b) Geometric filtering of Gaussian point cloud The reconstructed Gaussian point cloud may contain stray points due to background noise or artifacts. To achieve a cleaner model, we apply geometric filters to remove outliers, such as Gaussians far from the object centroid or with unusually large distances to their k nearest neighbors, as shown in the bottom-right section of Fig.2(d). After filtering, we resume Gaussian splatting training on the refined cloud for an additional 500 epochs to repair any discontinuities, further enhancing 3D reconstruction quality.

4. Experiments

In this section, we evaluate our method on both simulated and real on-sky data, comparing its 3D reconstruction performance with NeRF-based baseline approaches. We use standard imaging and 3D metrics—including SSIM, PSNR, LPIPS—to quantitatively assess reconstruction accuracy. Our method demonstrates superior reconstruction quality and robustness on both synthetic ground telescope satellite images and real observational data of China’s Space Station (CSS) and the International Space Station (ISS).

4.1. Simulation Results

Synthetic Ground Telescope Satellite Images For simulations, we created three distinct 3D satellite models in

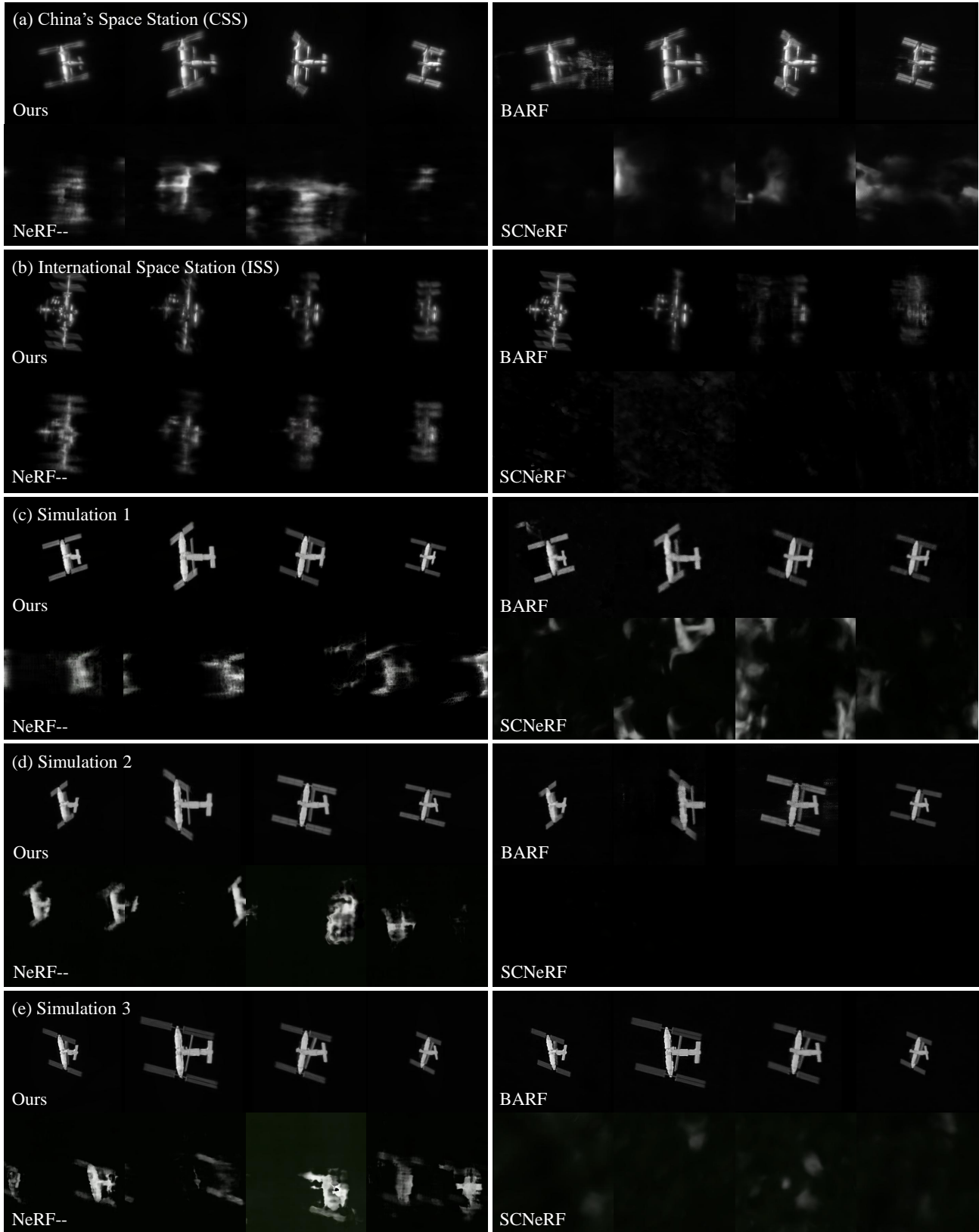


Figure 3. Comparison of 3D reconstruction and view synthesis results across different methods on real and simulated datasets, showing the robustness and clarity of our approach compared to NeRF-based methods (BARF, NeRF--, SCNeRF) across validation views.

Table 1. Comparison of our method with NeRF-based methods on three simulations and on-sky observations of China’s Space Station (CSS) and the International Space Station (ISS), showing validation view results. Best results are in **bold**, and second-best are underlined.

Method	Simulation 1			Simulation 2			Simulation 3			CSS			ISS		
	PSNR \uparrow	SSIM \uparrow	LPIPS \downarrow	PSNR \uparrow	SSIM \uparrow	LPIPS \downarrow	PSNR \uparrow	SSIM \uparrow	LPIPS \downarrow	PSNR \uparrow	SSIM \uparrow	LPIPS \downarrow	PSNR \uparrow	SSIM \uparrow	LPIPS \downarrow
Dirty Image	23.28	0.07	0.41	23.02	0.07	0.36	23.16	0.07	0.36	×	×	×	×	×	×
Pre-Processed	27.60	0.53	0.10	27.92	0.53	0.11	28.3	0.52	0.11	×	×	×	×	×	×
Ours	25.32	0.90	0.16	34.43	0.95	0.04	35.17	0.94	0.08	34.68	0.96	0.03	36.87	0.98	0.02
BARF	<u>22.63</u>	0.52	<u>0.19</u>	<u>30.26</u>	0.84	<u>0.08</u>	<u>27.49</u>	<u>0.82</u>	<u>0.16</u>	<u>31.04</u>	<u>0.87</u>	<u>0.06</u>	<u>31.53</u>	0.92	0.06
NeRF—	18.10	0.51	0.27	17.17	<u>0.85</u>	0.28	15.52	0.70	0.43	18.61	0.71	0.35	30.74	<u>0.93</u>	0.10
SCNeRF	18.19	<u>0.78</u>	0.37	18.75	<u>0.79</u>	0.39	19.28	0.69	0.34	17.62	0.75	0.27	18.14	<u>0.76</u>	0.38

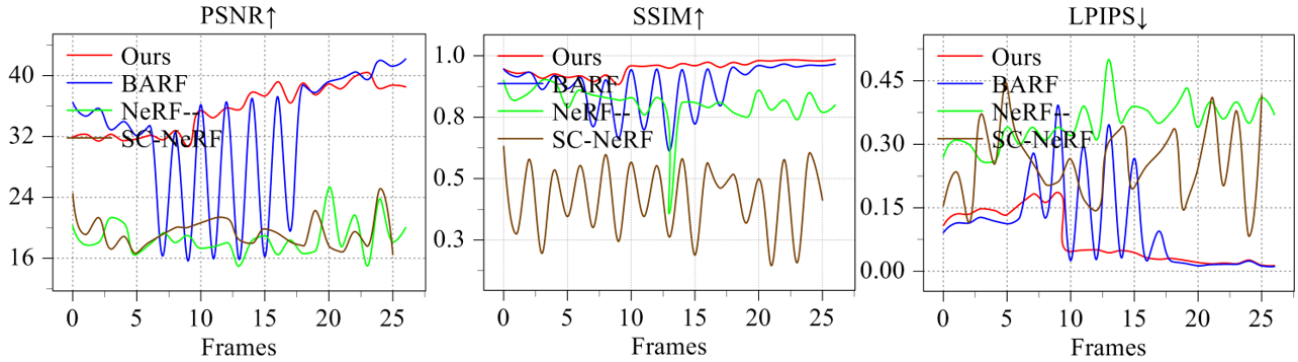


Figure 4. Imaging metrics evaluated across frames, covering both training and validation views, show that our method performs robustly across all data, while NeRF-based methods struggle with unseen viewpoints.

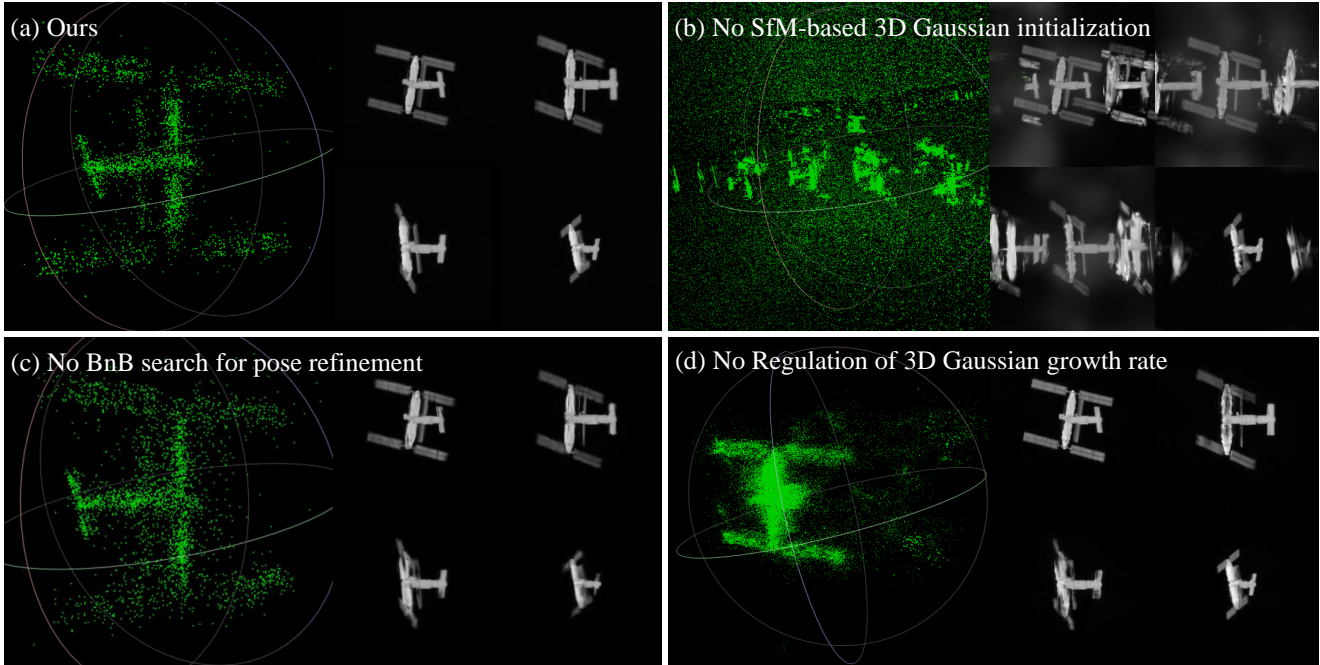


Figure 5. Ablation studies on the 1st simulation dataset. This figure showcases the impact of some components in our workflow on the reconstructed point clouds and novel view synthesis. (a) Results using our complete method. (b) Excluding SfM-based 3D Gaussian initialization introduces ghosting effects. (c) Excluding simultaneous pose refinement causes distortions and artifacts. (d) Excluding the regulation of 3D Gaussian growth rate also leads to distortions and artifacts.

Blender, producing datasets of ground telescope images for each. Each model, approximately 60 meters in size, was placed in a low-Earth orbit at 650 km altitude, resulting in a 13° segment of the full 360° trajectory observable by a stationary ground telescope. Our virtual telescope, with a 0.35-meter aperture and a 3.2-meter focal length, rendered 700 high-quality images per model. To simulate atmospheric conditions, each image was augmented with 20, introducing turbulence (with a Fried parameter between 0.07 and 0.35 meters) and light pollution (adding 5-7% background intensity), yielding a dataset of 14,000 distorted frames. This dataset will be publicly available upon the paper’s acceptance.

Implementation Details For preprocessing, we applied lucky imaging to select 148 high-quality images per model from 14,000 distorted frames. To validate preprocessing effectiveness, we compared post-processed images against ground truth, with results shown in Table 1. We subsequently selected one in every ten clean frames, resulting in a set of 15 training images, with the remainder reserved for validation. To ensure a fair comparison, camera poses for both our Gaussian splatting method and baseline methods (BARF, NeRF— and SCNeRF) were initialized using our improved SfM approach as described in Sec. 3.2.

3D Reconstruction Figure 3(c) shows 3D reconstruction results for the first simulation dataset, comparing our method with NeRF-based methods across selected views. NeRF-based methods struggle with certain views, generating unrealistic images, while our method maintains robust generalization across all validation views. This difference arises from the sampling strategies of NeRF variants versus 3D Gaussians; BARF’s uniform sampling can lead to global overfitting in sparse view conditions, whereas our Gaussian-based method refines local deformations to accurately capture the satellite’s 3D structure. The performance of our approach is further supported by the SSIM, PSNR, and LPIPS metrics across all frames and datasets, as illustrated in Fig.4(d) and Table 1. Our method also significantly reduces training time, reconstructing a 3D volume in approximately 4 minutes on a single NVIDIA RTX 4090—around 2 minutes for Gaussian splatting and 2 minutes for BnB pose refinement, compared to over 4 hours for BARF.

4.2. On-Sky Results

We applied our algorithm to real observations of China’s Tiangong Space Station (CSS) and the ISS, both low-Earth-orbit satellites with known geometric specifications, enabling us to assess our method’s accuracy by comparing the reconstructions with publicly available information.

Observations of CSS and ISS CSS was observed on September 15, 2023, from 20:48:30 to 20:51:17 UTC, near Miyun Reservoir, Beijing, China, with a closest approach of



Figure 6. An official image of the Chinese Space Station (CSS) with the imaging instrument shown in the lower right corner: a Celestron C14HD telescope paired with a QHY5III678M planetary camera. The CSS comprises four primary modules: 1 - Tianhe Core Module, 2 - Mengtian Laboratory Module, 3 - Wentian Laboratory Module, 4 - Tianzhou-6 Cargo Spacecraft.

389.4 km and a peak elevation of 78.3° . ISS was observed on August 21, 2024, from 20:20:06 to 20:22:09 UTC at the Yanqing District, Beijing, China, with a closest approach of 442 km and a peak elevation of 86° . For both observations, we used a Celestron C14HD telescope (0.35 m diameter, f/11) with a QHY5III678M camera (as shown in upper right corner of Fig.6), achieving a spatial sampling rate of 0.106 arcsec/pixel and an approximate resolution of 0.2 m/pixel. Observations utilized the “Fake Polar Axis Method” with a German-type equatorial mount (CGX-L), uniquely oriented not towards the north but towards a precisely calculated azimuth relative to the apparent track of the space object. This innovative design prevented the need for a meridian flip during the observation and minimized field rotation, particularly beneficial for the central part of the image sequence. Images were captured at 5 ms exposures, averaging 88 fps for CSS and 55 fps for ISS, resulting in datasets of 13,800 images for CSS and 6,770 for ISS.

Implementation Details Using lucky imaging, we selected 138 clean frames for CSS and 116 clean frames for ISS from the initial raw images. As in the simulation, we selected one image from every ten for training (totaling 15 images for CSS and 12 for ISS) and set aside the rest for validation. Our method was benchmarked against three NeRF baselines, BARF, NeRF—, and SC-NeRF. In the absence of ground-truth images for on-sky data, we compared reconstructed images with pre-processed inputs and validated metrology results.

3D Reconstruction and Metrology The 3D reconstruction results for CSS and ISS (Fig.3) mirror our simulation

Table 2. Ablation study on three simulated data. For clarity, the results in the table represent novel view synthesis outcomes, with the optimal result in each column highlighted in **bold** and the second-best result underlined.

Method	Simulation 1			Simulation 2			Simulation 3		
	PSNR [↑]	SSIM [↑]	LPIPS [↓]	PSNR [↑]	SSIM [↑]	LPIPS [↓]	PSNR [↑]	SSIM [↑]	LPIPS [↓]
Ours	25.33	0.90	0.16	36.89	0.96	0.03	<u>35.25</u>	0.95	0.07
No Sharpening	<u>25.04</u>	<u>0.89</u>	0.19	32.42	0.53	0.02	36.64	0.54	0.01
No Gaussian initialization	18.10	<u>0.89</u>	0.25	18.63	0.57	0.22	18.85	0.57	0.25
No pose refinement	22.51	0.86	0.18	29.93	0.65	0.06	33.80	0.63	0.07
No Regulation of Gaussian	22.98	0.87	0.14	29.54	0.76	0.04	34.98	<u>0.94</u>	<u>0.06</u>
No Point cloud Filtering	24.98	0.62	0.17	<u>34.75</u>	<u>0.94</u>	0.05	35.10	<u>0.94</u>	0.08

Table 3. Metrology of the China’s Space Station modules and their solar wings.

	Measured	GT[48]
Length		
Tianhe Core Module	16.11	16.6
Mengtian Laboratory	17.30	17.88
Wentian Laboratory	17.30	17.88
Tianzhou-6	9.71	10.6
Diameter		
Tianhe Core Module	5.65	4.2
Mengtian Module	5.50	4.2
Wentian Module	5.63	4.2
Tianzhou 6	3.30	3.35
The length of the solar wings		
Tianhe Core Module	25.44	×
Mengtian Laboratory Module	55.62	55
Wentian Laboratory Module	55.62	55
Tianzhou 6	4.89	×
Solar wing angle		
Tianhe Core Module	0.78	×
Mengtian Laboratory Module	63.01	×
Wentian Laboratory Module	68.71	×
Tianzhou-6	3.22	×

findings. BARF and other NeRF variants struggled to render unseen views when training data were limited, while our approach accurately captured the satellites’ 3D structures. This performance difference is further supported by the image quality metrics shown in Table 1. For detailed metrology, we measured the dimensions of four CSS modules (Tianhe, Mengtian, Wentian, and Tianzhou-6) and the angles and lengths of their solar arrays, as shown in Fig.6. Using our 3D Gaussian splatting-reconstructed volume, we densely sampled 2D views, identifying frames where each module reached its maximum length in orthogonal perspectives and determining dimensions through pixel counts. The

angles of the solar arrays were calculated based on their relative positions to the station’s main modules. These metrology results, outlined in Table 3, align closely with officially released specifications.

4.3. Ablation Study

Comprehensive ablation studies were carried out to ascertain the necessity of each element within our 3D reconstruction framework. Fig.7 showcases the consequences of excluding particular components from our pipeline, displaying the reconstructed points on the left and representative rendered views on the right for each subplot. The components omitted are wavelet decomposition sharpening (Sec.3.1.b), SfM-based 3D Gaussian initialization (Sec.3.2), BnB search for pose refinement (Sec.3.3.a), regulation of 3D Gaussian growth rate (Sec.3.3.a, splitting large Gaussians every 100 epochs instead of 500 epochs), and point cloud filtering (Sec.3.3.b). The exclusion of these steps visibly impairs the reconstruction outcome, manifesting as blurriness, ghosting, fringe artifacts, and unclear backgrounds, among other issues. Furthermore, Table 2 details the quantitative results of these ablation studies, underscoring the degradation in reconstruction quality when vital steps are skipped. The ablation results for lucky imaging (Sec.3.1.a) and feature annotation (Sec.3.2.a) are not presented, as omitting these steps resulted in the inability to reconstruct anything.

5. Conclusion

In this paper, we present a novel 3D imaging framework for reconstructing satellites from ground telescope observations. Central to this framework is a customized Structure from Motion (SfM) and advanced Gaussian splatting volume rendering, supported by sophisticated pre-processing, simultaneous pose refinement, and post-editing to manage distortions from atmospheric turbulence, light pollution, unique camera characteristics, and other factors. We validated our method on synthetic datasets and real observations of China’s Tiangong Space Station and the International Space Station.

Our work provides practical insights into ground-based 3D reconstruction, offering a cost-effective alternative to space-based surveillance by reducing monitoring costs and improving accessibility for satellite and debris observation. However, a major limitation of our current methodology is the overly complex operational workflow and the difficulty in achieving reliable reconstruction with extremely low-quality images. To address this, future work will focus on developing a fully automated, end-to-end workflow—from video capture to 3D model generation—while enhancing robustness to handle challenging imaging conditions, thereby broadening the applicability of ground-based satellite reconstruction.

References

- [1] Nantheera Anantrasirichai, Alin Achim, Nick G Kingsbury, and David R Bull. Atmospheric turbulence mitigation using complex wavelet-based fusion. *IEEE Transactions on Image Processing*, 22(6):2398–2408, 2013. 2
- [2] Nantheera Anantrasirichai, Alin Achim, and David Bull. Atmospheric turbulence mitigation for sequences with moving objects using recursive image fusion. In *IEEE international conference on image processing*, pages 2895–2899, 2018. 2
- [3] Cor Berrevoets. Registax 6. <http://www.astronomie.be/registax/>, 2011. Version 6.1.0.8. 4, 1
- [4] Ang Cao and Justin Johnson. Hexplane: A fast representation for dynamic scenes. In *Proceedings of the IEEE/CVF Conference on Computer Vision and Pattern Recognition*, pages 130–141, 2023. 2
- [5] Anpei Chen, Zexiang Xu, Andreas Geiger, Jingyi Yu, and Hao Su. Tensorf: Tensorial radiance fields. In *European Conference on Computer Vision (ECCV)*, 2022. 2
- [6] Yiwen Chen, Zilong Chen, Chi Zhang, Feng Wang, Xiaofeng Yang, Yikai Wang, Zhongang Cai, Lei Yang, Huaping Liu, and Guosheng Lin. Gaussianeditor: Swift and controllable 3d editing with gaussian splatting. *arXiv preprint arXiv:2311.14521*, 2023. 2
- [7] Nicholas Chimitt, Xingguang Zhang, Zhiyuan Mao, and Stanley H Chan. Real-time dense field phase-to-space simulation of imaging through atmospheric turbulence. *IEEE Transactions on Computational Imaging*, 8:1159–1169, 2022. 2
- [8] Kaitlin Dennison and Simone D’Amico. Vision-based 3d reconstruction for navigation and characterization of unknown, space-borne targets. *Austin, TX, Jan*, 2023. 2
- [9] Daniel DeTone, Tomasz Malisiewicz, and Andrew Rabynovich. Superpoint: Self-supervised interest point detection and description. In *Proceedings of the IEEE conference on computer vision and pattern recognition workshops*, pages 224–236, 2018. 4
- [10] Simone D’Amico, Mathias Benn, and John L Jørgensen. Pose estimation of an uncooperative spacecraft from actual space imagery. *International Journal of Space Science and Engineering* 5, 2(2):171–189, 2014. 2
- [11] Jiemin Fang, Junjie Wang, Xiaopeng Zhang, Lingxi Xie, and Qi Tian. Gaussianeditor: Editing 3d gaussians delicately with text instructions. *arXiv preprint arXiv:2311.16037*, 2023. 2
- [12] Martin A Fischler and Robert C Bolles. Random sample consensus: a paradigm for model fitting with applications to image analysis and automated cartography. *Communications of the ACM*, 24(6):381–395, 1981. 2
- [13] Sara Fridovich-Keil, Giacomo Meanti, Frederik Rahbæk Warburg, Benjamin Recht, and Angjoo Kanazawa. K-planes: Explicit radiance fields in space, time, and appearance. In *Proceedings of the IEEE/CVF Conference on Computer Vision and Pattern Recognition*, pages 12479–12488, 2023. 2
- [14] Chris Garry. Pipp: Planetary imaging preprocessor. <https://sites.google.com/site/astropipp/>, 2014. Version 2.3.8. 4
- [15] Jiajun Huang and Hongchuan Yu. Point’n move: Interactive scene object manipulation on gaussian splatting radiance fields. *arXiv preprint arXiv:2311.16737*, 2023. 2
- [16] Yoonwoo Jeong, Seokjun Ahn, Christopher Choy, Anima Anandkumar, Minsu Cho, and Jaesik Park. Self-calibrating neural radiance fields. In *Proceedings of the IEEE/CVF International Conference on Computer Vision*, pages 5846–5854, 2021. 2
- [17] Laura F Julià, Pascal Monasse, and Marc Pierrot-Deseilligny. The orthographic projection model for pose calibration of long focal images. *Image Processing On Line*, 9:231–250, 2019. 4, 1
- [18] Bernhard Kerbl, Georgios Kopanas, Thomas Leimkühler, and George Drettakis. 3d gaussian splatting for real-time radiance field rendering. *ACM Transactions on Graphics*, 42(4), 2023. 2
- [19] Emil Kraaikamp. Autostakkert! Software available from AutoStakkert website, 2024. Accessed: 2024-03-20. 4, 1
- [20] Ailsa H Land and Alison G Doig. *An automatic method for solving discrete programming problems*. Springer, 2010. 4
- [21] Nicholas M Law, Craig D Mackay, and John E Baldwin. Lucky imaging: high angular resolution imaging in the visible from the ground. *Astronomy & Astrophysics*, 446(2): 739–745, 2006. 2
- [22] Jingyun Liang, Jiezhong Cao, Yuchen Fan, Kai Zhang, Rakesh Ranjan, Yawei Li, Radu Timofte, and Luc Van Gool. Vrt: A video restoration transformer. *arXiv preprint arXiv:2201.12288*, 2022. 4
- [23] Chen-Hsuan Lin, Wei-Chiu Ma, Antonio Torralba, and Simon Lucey. Barf: Bundle-adjusting neural radiance fields. In *Proceedings of the IEEE/CVF international conference on computer vision*, pages 5741–5751, 2021. 2
- [24] David G Lowe. Object recognition from local scale-invariant features. In *Proceedings of the seventh IEEE international conference on computer vision*, pages 1150–1157. Ieee, 1999. 2
- [25] David G Lowe. Distinctive image features from scale-invariant keypoints. *International journal of computer vision*, 60:91–110, 2004. 2
- [26] Zhiyuan Mao, Nicholas Chimitt, and Stanley H Chan. Image reconstruction of static and dynamic scenes through anisoplanatic turbulence. *IEEE Transactions on Computational Imaging*, 6:1415–1428, 2020. 2

- [27] Zhiyuan Mao, Nicholas Chimitt, and Stanley H Chan. Accelerating atmospheric turbulence simulation via learned phase-to-space transform. In *Proceedings of the IEEE/CVF International Conference on Computer Vision*, pages 14759–14768, 2021. 2
- [28] Kangfu Mei and Vishal M Patel. Ltt-gan: Looking through turbulence by inverting gans. *IEEE Journal of Selected Topics in Signal Processing*, 2023. 2
- [29] Ben Mildenhall, Pratul P Srinivasan, Matthew Tancik, Jonathan T Barron, Ravi Ramamoorthi, and Ren Ng. Nerf: Representing scenes as neural radiance fields for view synthesis. *Communications of the ACM*, 65(1):99–106, 2021. 2
- [30] Thomas Müller, Alex Evans, Christoph Schied, and Alexander Keller. Instant neural graphics primitives with a multiresolution hash encoding. *ACM Trans. Graph.*, 41(4):102:1–102:15, 2022. 2
- [31] Tae Ha Park and Simone D’Amico. Rapid abstraction of spacecraft 3d structure from single 2d image. In *AIAA SCITECH 2024 Forum*, page 2768, 2024. 2
- [32] Tae Ha Park and Simone D’Amico. Adaptive neural-network-based unscented kalman filter for robust pose tracking of noncooperative spacecraft. *Journal of Guidance, Control, and Dynamics*, 46(9):1671–1688, 2023. 2
- [33] Tae Ha Park and Simone D’Amico. Robust multi-task learning and online refinement for spacecraft pose estimation across domain gap. *Advances in Space Research*, 2023. 2
- [34] Tae Ha Park, Marcus Märten, Gurvan Lecuyer, Dario Izzo, and Simone D’Amico. Speed+: Next-generation dataset for spacecraft pose estimation across domain gap. In *2022 IEEE Aerospace Conference (AERO)*, pages 1–15. IEEE, 2022. 2
- [35] Sijia Qiao, Haopeng Zhang, Gang Meng, Meng An, Fengying Xie, and Zhiguo Jiang. Deep-learning-based satellite relative pose estimation using monocular optical images and 3d structural information. *Aerospace*, 9(12):768, 2022. 2
- [36] Shyam Nandan Rai and CV Jawahar. Removing atmospheric turbulence via deep adversarial learning. *IEEE Transactions on Image Processing*, 31:2633–2646, 2022. 2
- [37] François Roddier. Adaptive optics in astronomy. 1999. 2
- [38] Paul-Edouard Sarlin, Daniel DeTone, Tomasz Malisiewicz, and Andrew Rabinovich. Superglue: Learning feature matching with graph neural networks. In *Proceedings of the IEEE/CVF conference on computer vision and pattern recognition*, pages 4938–4947, 2020. 4
- [39] Johannes L Schonberger and Jan-Michael Frahm. Structure-from-motion revisited. In *Proceedings of the IEEE conference on computer vision and pattern recognition*, pages 4104–4113, 2016. 2
- [40] Armin Schwartzman, Marina Alterman, Rotem Zamir, and Yoav Y Schechner. Turbulence-induced 2d correlated image distortion. In *IEEE International Conference on Computational Photography*, pages 1–13, 2017. 2
- [41] Sumant Sharma and Simone D’Amico. Neural network-based pose estimation for noncooperative spacecraft rendezvous. *IEEE Transactions on Aerospace and Electronic Systems*, 56(6):4638–4658, 2020. 2
- [42] Sumant Sharma, Jacopo Ventura, and Simone D’Amico. Robust model-based monocular pose initialization for noncooperative spacecraft rendezvous. *Journal of Spacecraft and Rockets*, 55(6):1414–1429, 2018. 2
- [43] Sumant Sharma et al. Comparative assessment of techniques for initial pose estimation using monocular vision. *Acta Astronautica*, 123:435–445, 2016. 2
- [44] John D. Smith and Jane Doe. A review of space surveillance techniques and 3d reconstruction applications. *International Journal of Space Science*, 45:123–145, 2020. 2
- [45] SpaceX. Starlink. <https://www.starlink.com>. Accessed: [November, 2024]. 1
- [46] Bill Triggs, Philip F McLauchlan, Richard I Hartley, and Andrew W Fitzgibbon. Bundle adjustment—a modern synthesis. In *Vision Algorithms: Theory and Practice: International Workshop on Vision Algorithms Corfu, Greece, September 21–22, 1999 Proceedings*, pages 298–372. Springer, 2000. 2
- [47] Zirui Wang, Shangzhe Wu, Weidi Xie, Min Chen, and Victor Adrian Prisacariu. Nerf-: Neural radiance fields without known camera parameters. *arXiv preprint arXiv:2102.07064*, 2021. 2
- [48] Wikipedia. Tiangong space station, 2024. [Online; accessed 28-March-2024]. 8
- [49] Rajeev Yasarla and Vishal M Patel. Learning to restore images degraded by atmospheric turbulence using uncertainty. In *2021 IEEE International Conference on Image Processing*, pages 1694–1698, 2021. 2
- [50] Haopeng Zhang, Quanmao Wei, and Zhiguo Jiang. 3d reconstruction of space objects from multi-views by a visible sensor. *Sensors*, 17(7):1689, 2017. 2
- [51] Xin Zhang, Zhiguo Jiang, Haopeng Zhang, and Quanmao Wei. Vision-based pose estimation for textureless space objects by contour points matching. *IEEE Transactions on Aerospace and Electronic Systems*, 54(5):2342–2355, 2018. 2
- [52] Xingguang Zhang, Nicholas Chimitt, Yiheng Chi, Zhiyuan Mao, and Stanley H Chan. Spatio-temporal turbulence mitigation: A translational perspective. *arXiv preprint arXiv:2401.04244*, 2024. 2

Reconstructing Satellites in 3D from Amateur Telescope Images

Supplementary Material

6. Pre-processing

Our image processing workflow begins by selecting the top 12% of frames from an image series based on sharpness and clarity. These high-quality frames are then aligned by detecting high-contrast features to correct for atmospheric turbulence. Once aligned, the frames are stacked by averaging pixel values across frames, which reduces noise and enhances detail, resulting in a smoother but slightly softer image. To sharpen the image further, we then proceed with an enhancement process. The stacked image is subjected to wavelet transformation, decomposing its frequency components into six levels. We adjust the frequency weights of each level to refine various details, then recombine the modified frequency layers to create a clearer, sharper final image. The stacking phase is achieved using AutoStakkert[19], while the sharpening phase is completed using RegiStax 6[3]. The comparative results of these pre-processing methods are presented in Table 4.

7. Satellite’s Pose and Shape Initialization

7.1. Pose initialization with orthographic projection

In our work, the initial pose estimation for long focal length images builds upon the orthographic projection model described by Julià et al. (2019)[17]. This method approximates the perspective camera model with the scaled orthographic model when the camera is far from the scene relative to its size. Using the scaled orthographic projection function:

$$\rho_{SO} : X \mapsto x = \frac{f}{\mathbf{k}^\top O + t_z} \left[\begin{pmatrix} \mathbf{i}^\top \\ \mathbf{j}^\top \end{pmatrix} X + \begin{pmatrix} t_x \\ t_y \end{pmatrix} \right] + \begin{pmatrix} c_x \\ c_y \end{pmatrix}, \quad (1)$$

where X represents a 3D point in the scene, O is the centroid of the scene, and $(\mathbf{i}, \mathbf{j}, \mathbf{k})$ are the axes of the projection. The parameters t_x, t_y, t_z represent the translation components of the camera, with t_z denoting the distance between the camera and the scene along the optical axis. The terms c_x, c_y are the 2D coordinates of the principal point (the image center) in the camera frame. The relationship between the pose parameters (R, T) , which transform points from the camera coordinate system to the world coordinate system, and the scaled orthographic projection is defined as:

$$R = \begin{pmatrix} \mathbf{i}^\top \\ \mathbf{j}^\top \\ \mathbf{k}^\top \end{pmatrix}, \quad T = \begin{pmatrix} t_x \\ t_y \\ t_z \end{pmatrix}. \quad (2)$$

The 3D points X and the pose parameters R and T are

determined using the Tomasi-Kanade Factorization. This method relies on the Equation 1, the 2D projection matrix x , the focal length f , and the orthogonal relationship among the vectors \mathbf{i}, \mathbf{j} , and \mathbf{k} . For more details, refer to [17].

7.2. Customized SfM with temporal continuity

Given the initial poses (R and T) of the first three images, along with the corresponding 3D point cloud (X) and the feature point correspondences between adjacent images, the following procedure is performed to incorporate additional images into the reconstruction process sequentially:

1. A new image is added to the sequence in the order it was captured. Using feature point correspondences with adjacent images, the 3D points for the new image’s feature points are estimated.

2. The pose (R and T) of the newly added image is determined using the Perspective-n-Point (PnP) algorithm, which minimizes the reprojection error between the observed 2D feature points (x_i) and their projections (\hat{x}_i) based on the estimated pose and 3D points (X_i):

$$(R, T) = \arg \min_{R, T} \sum_{i=1}^n \|x_i - K(RX_i + T)\|^2, \quad (3)$$

where K is the intrinsic camera matrix and n is the number of feature correspondences.

3. All 3D points and camera poses, including those of the newly added image, are refined by minimizing the overall reprojection error across all images and points. To account for visibility, a visibility function $\text{vis}(k, j)$ is introduced, which equals 1 if the j -th 3D point is visible in the k -th image, and 0 otherwise:

$$(R_k, T_k, X_j) = \arg \min_{R_k, T_k, X_j} \sum_{k=1}^m \sum_{j=1}^n \text{vis}(k, j) \cdot \|x_{kj} - \hat{x}_{kj}\|^2, \quad (4)$$

where $\hat{x}_{kj} = K(R_k X_j + T_k)$ is the reprojection of the j -th point in the k -th image, m is the number of images, and n is the number of 3D points.

Steps 1, 2, and 3 are repeated for each additional image until all images have been incorporated into the reconstruction.

Furthermore, approximately every 5 iterations, triangulation is performed between two adjacent images to expand the 3D point cloud by adding new points, enhancing the density and accuracy of the reconstruction.

Table 4. Performance comparison of different preprocessing methods on simulated data. The table shows the progressive improvement in novel view synthesis quality across various stages of preprocessing. The best result in each column is highlighted in **bold**, and the second-best result is underlined.

Method	Dataset 1			Dataset 2			Dataset 3		
	PSNR [↑]	SSIM [↑]	LPIPS [↓]	PSNR [↑]	SSIM [↑]	LPIPS [↓]	PSNR [↑]	SSIM [↑]	LPIPS [↓]
Simulated Data	23.28	0.07	0.41	23.02	0.07	0.36	23.16	0.07	0.36
Stacked Images	27.00	0.41	0.15	27.15	0.41	0.17	27.75	0.41	0.16
Sharpened Images	<u>27.60</u>	0.53	0.10	<u>27.92</u>	<u>0.53</u>	0.11	<u>28.3</u>	<u>0.52</u>	<u>0.11</u>
After VRT	27.74	<u>0.45</u>	<u>0.11</u>	28.02	0.55	<u>0.13</u>	28.47	0.54	0.11

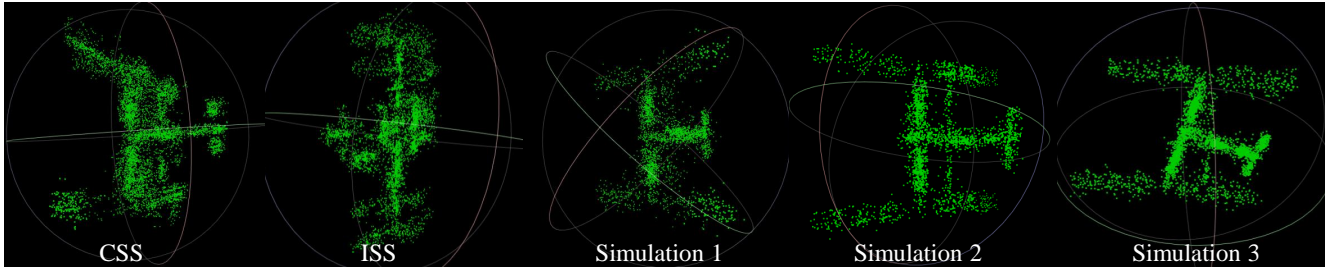


Figure 7. Point clouds reconstructed from five datasets, including two real-world datasets (CSS and ISS) and three simulation datasets (Simulation 1, Simulation 2, and Simulation 3). The datasets vary in complexity and geometry, highlighting the reconstruction capabilities under different scenarios.

8. Joint pose refinement and Post-editing

8.1. Branch and Bound (BnB) for Pose Refinement

Our method employs the Branch and Bound (BnB) algorithm for pose optimization, with the Gaussian Splatting model held fixed during each BnB iteration. The BnB framework refines the rotation matrix R and translation vector T . To achieve optimal alignment between observed images and the Gaussian Splatting model, we leverage geometric (or photometric) consistency across multiple images. Unlike traditional BnB, which continuously subdivides the solution space, our approach alternates between pose optimization and Gaussian Splatting model reconstruction. After each pose optimization, the updated pose is used to improve the Gaussian Splatting model, with this alternation continuing for a set number of reconstruction rounds before resuming pose refinement. This iterative process efficiently converges to a globally optimal pose estimate.

8.1.1. Problem Formulation

Our objective is to find the optimal R and T that minimize the projection error between observed images I_i and rendered images $G(R_i, T_i)$ from the Gaussian Splatting model. We define the Gaussian Splatting Loss (\mathcal{L}_{GS}) as:

$$\mathcal{L}_{GS}(I, G) = \sigma \|I - G\|_1 + (1 - \sigma) \cdot \text{SSIM}(I, G), \quad (5)$$

where σ is a weighting parameter balancing the contributions of the L_1 loss and the SSIM loss.

Using this loss function, the optimization objective is reformulated as:

$$\min_{R_i, T_i} \sum_{i=1}^n \mathcal{L}_{GS}(I_i, G(R_i, T_i)), \quad (6)$$

where: I_i is the i -th observed image, R_i and T_i are the pose parameters for image I_i , and $G(R_i, T_i)$ is the rendered image generated from the fixed Gaussian Splatting model using pose (R_i, T_i) .

The goal is to determine (R_i, T_i) for each image to minimize the Gaussian Splatting Loss, achieving optimal alignment between observed and rendered images.

8.1.2. BnB Framework for Pose Refinement

The BnB framework iteratively refines candidate poses to achieve convergence on R and T . The process includes the following steps:

1. Initialization:

Initial estimates for R and T are obtained from Section 3.2, which provides approximate poses from initial observations. These values serve as the starting point for BnB optimization.

2. Branch (Subdivision):

Candidate poses are generated by introducing controlled perturbations in both rotation and translation:

- A random rotation angle $\Delta\theta$ is drawn from a uniform distribution in $[0, \theta_{\max}]$, with a random rotation axis \vec{n} .

The rotation perturbation R_{noise} is computed using Rodrigues' rotation formula:

$$R_{\text{noise}} = I + \sin(\Delta\theta)[\vec{n}]_{\times} + (1 - \cos(\Delta\theta))[\vec{n}]_{\times}^2, \quad (7)$$

where $[\vec{n}]_{\times}$ is the skew-symmetric matrix of \vec{n} .

- The translation perturbation T_{noise} is sampled from a Gaussian distribution centered at zero:

$$T_{\text{noise}} \sim \mathcal{N}(0, \sigma_T^2), \quad (8)$$

Candidate rotation matrices $\{R_i\}$ and translation vectors $\{T_i\}$ are generated as:

$$R_i = R \cdot R_{\text{noise}}, \quad T_i = T + T_{\text{noise}}, \quad (9)$$

forming a set of candidate poses $\{(R_i, T_i)\}$ for evaluation.

3. Error Estimation and Optimal Pose Selection:

For each candidate pose (R_i, T_i) , we calculate the projection error as:

$$E(R_i, T_i) = \mathcal{L}_{\text{GS}}(I_i, G(R_i, T_i)), \quad (10)$$

The pose with the minimum error, $(R_{\text{best}}, T_{\text{best}})$, is selected:

$$R_{\text{best}}, T_{\text{best}} = \arg \min_{(R_i, T_i)} E(R_i, T_i), \quad (11)$$

If $E(R_{\text{best}}, T_{\text{best}})$ improves upon the current best error E_{best} , $(R_{\text{best}}, T_{\text{best}})$ is adopted as the updated pose.

4. Iteration and Convergence:

The optimization alternates between Gaussian Splatting model reconstruction and BnB-based pose refinement. After a fixed number of reconstruction rounds, BnB refines the pose with successively smaller perturbations in R and T . The process terminates after performing a total of 10 BnB iterations, ensuring sufficient refinement across all pose parameters.

The final pose $(R^*, T^*) = (R_{\text{best}}, T_{\text{best}})$ is the pose that minimizes the projection error:

$$(R^*, T^*) = \arg \min_{R_i, T_i} E(R_i, T_i) \quad (12)$$

This alternating optimization with progressively smaller perturbations ensures convergence to a globally optimal pose consistent with observed images.

8.2. Post-editing

Image noise and distortions often lead to a significant presence of discrete noise points in 3D structures reconstructed with Gaussian Splatting, which contradicts the understanding that satellite structures are continuous. To mitigate this issue, we implemented a two-step filtering process to effectively eliminate these noise points.

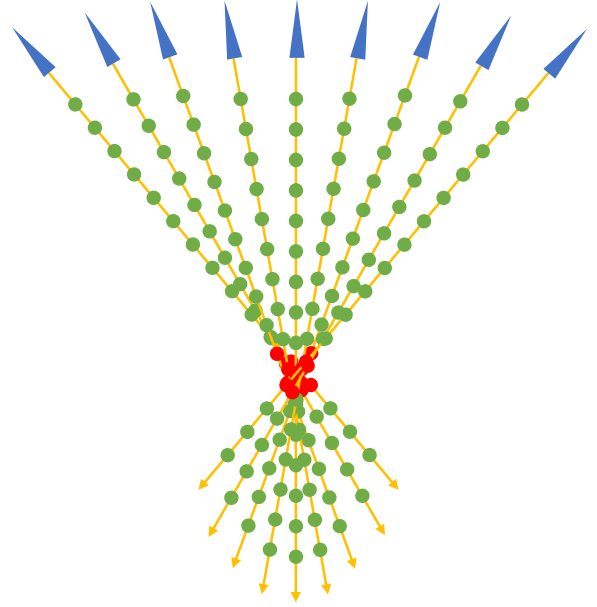


Figure 8. Custom NeRF sampling strategy. Blue triangles indicate cameras, yellow rays are light rays, green circles show uniform sampling points, and red circles reflect our tailored sampling based on camera distance to the point cloud center.

First, we computed the center and maximum radius of the initial point cloud, which was obtained from the customized Structure from Motion (SfM) process (Sec.3.2). Points in the reconstructed cloud that exceeded 1.2 times this maximum radius from the center were directly discarded, ensuring that only points within a reasonable spatial range were retained.

Second, we applied a statistical outlier filter to further refine the point cloud by eliminating isolated noise points that were significantly distant from their neighbors. This method, visualized in the right bottom of Fig. 2(d), identifies outliers based on the average distance \bar{d}_i of each point to its k -nearest neighbors. Using the mean (μ) and standard deviation (σ) of these distances across the point cloud, we defined a threshold $\tau = \mu + \alpha \cdot \sigma$, where α is a multiplier (set to 1 in our implementation). Points with $\bar{d}_i > \tau$ were flagged as outliers and removed.

This two-step process ensures that the reconstructed 3D structure better aligns with the expected continuous distribution of satellite components, significantly reducing noise while preserving essential geometric details.

9. Experimental Details

9.1. Ground Truth for Simulated Data

For simulated data, the ground truth (GT) refers to images that are free of atmospheric turbulence and noise. These

idealized images serve as the baseline for evaluating the quality of processed and rendered images.

9.2. Image Alignment and Quality Metrics

Camera motion during simulated image acquisition, subsequent centering adjustments, and pose interpolation can lead to misalignment between processed or rendered validation images and the ground truth. We employ a sliding alignment approach to address this issue when calculating metrics such as PSNR, SSIM, and LPIPS. First, the ground truth image is extended with a significant black border to allow for sliding comparisons. The processed or rendered image is then matched against the extended ground truth by sliding over it to locate the region with the smallest L_2 loss. Once the best-matching region is identified, the ground truth is cropped to align with the image, and the metrics are calculated on the aligned images. This method ensures a fair and consistent evaluation for both processed and rendered images.

9.3. Customized Sampling for NeRF

NeRF is susceptible to overfitting with long focal lengths and sparse viewpoints. To address this, we precisely tailor the sampling ranges (**near** and **far**) for each camera based on its distance from the point cloud center, ensuring accurate sampling and minimizing overfitting.

In Fig. 8, blue triangles represent the cameras, while yellow rays indicate the light rays emitted from each camera. The green circles depict the traditional NeRF sampling points, which apply the same **near** and **far** ranges to all cameras and are more prone to overfitting in sparse views.

To improve this, we use distances derived from our customized Structure-from-Motion (SfM) results to calculate the **near** and **far** ranges for each camera, as shown by the red circles in Fig. 8. This customized sampling strategy enhances reconstruction robustness, even in challenging scenarios with sparse viewpoints and long focal lengths.